

Article

Analysis of Bulb Turbine Hydrofoil Cavitation

Andrej Podnar, Marko Hočevar, Lovrenc Novak  and Matevž Dular * 

Faculty of Mechanical Engineering, University of Ljubljana, Aškerčeva 6, 1000 Ljubljana, Slovenia; andrej.podnar@gmail.com (A.P.); marko.hocevar@fs.uni-lj.si (M.H.); lovrenc.novak@fs.uni-lj.si (L.N.)
* Correspondence: matevz.dular@fs.uni-lj.si; Tel.: +386-1-477-1453

Featured Application: Bulb water turbine blades with improved cavitation properties.

Abstract: The influence of a bulb runner blade hydrofoil shape on flow characteristics around the blade was studied. Experimental work was performed on a bulb turbine measuring station and a single hydrofoil in a cavitating tunnel. In the cavitation tunnel, flow visualization was performed on the hydrofoil's suction side. Cavitation structures were observed for several cavitation numbers. Cavitation was less intense on the modified hydrofoil than on the original hydrofoil, delaying the cavitation onset by several tenths in cavitation number. The results of the visualization in the cavitation tunnel show that modifying the existing hydrofoil design parameters played a key role in reducing the cavitation inception and development, as well as the size of the cavitation structures. A regression model was produced for cavitation cloud length. The results of the regression model show that cavitation length is dependent on Reynolds's number and the cavitation number. The coefficients of determination for both the existing and modified hydrofoils were reasonably high, with R^2 values above 0.95. The results of the cavitation length regression model also confirm that the modified hydrofoil exhibits improved the cavitation properties.

Keywords: hydrofoil; bulb turbine; bulb turbine runner; cavitation; flow visualization; cavitation tunnel; regression model



Citation: Podnar, A.; Hočevar, M.; Novak, L.; Dular, M. Analysis of Bulb Turbine Hydrofoil Cavitation. *Appl. Sci.* **2021**, *11*, 2639. <https://doi.org/10.3390/app11062639>

Academic Editor: Florent Ravelet

Received: 12 February 2021
Accepted: 10 March 2021
Published: 16 March 2021

Publisher's Note: MDPI stays neutral with regard to jurisdictional claims in published maps and institutional affiliations.



Copyright: © 2021 by the authors. Licensee MDPI, Basel, Switzerland. This article is an open access article distributed under the terms and conditions of the Creative Commons Attribution (CC BY) license (<https://creativecommons.org/licenses/by/4.0/>).

1. Introduction

Historically, hydropower was used as a source of baseload generation for electric power, but now it is increasingly used for grid balancing. Among dispatchable renewable energy sources, hydropower plants are the most often used [1], achieving up to 15 s response times [2] for 90% of the total power response. The future potential of hydropower is shifting towards grid regulation tasks. Including nondispatchable renewable energy sources, e.g., inter alia wind and photovoltaics, and market deregulation, creates the requirement for rapid power generation fluctuations and power increase in the afternoon [3–5]. Any new hydraulic turbine design should therefore enable this type of operation and reach high efficiency and stable operation outside its optimal operating interval. Besides stable continuous turbine operation away from the best efficiency point, new designs will also need to function sufficiently in transient operation. Bulb turbines face challenges for such operation; designers will have to overcome the detrimental effects that flow fluctuations and cavitation have on turbine operation, while still ensuring adequate performance over a broad interval of operating points and in transient operation [3].

At the best efficiency point, an optimal combination of the runner frequency of the rotation, head, and discharge is available. At such an operating point, flow separation is usually low, and no cavitation is observed. For operation away from the optimum efficiency point, bulb turbines, as compared e.g., to Francis turbines [4], feature double regulation and may operate in a wide interval of operating conditions with reasonably high efficiency. Although all hydraulic turbine types are constantly improved, the gains in efficiency are in the per mille range and the cavitation in hydraulic turbines remains an

issue. The cavitation in the hydraulic turbines [4,6,7] decreases efficiency and increases vibrations and erosion, thereby reducing the service life.

The procedures optimizing the performance of turbine hydraulics are most often based on the use of so-called inverse design methods [8] and computational fluid dynamics (CFD) [9].

Inverse design methods have been in use for decades, with the first 3D methods emerging around 30 years ago. These methods are based on the a priori specification of the pressure or blade loading distribution. Such distribution along the runner blade in the radial and meridional directions facilitates the calculation of the runner blade's angle. This reduces the computational CFD work required when insufficient information on the runner geometry is known in advance. Zangeneh [10] proposed a three-dimensional design method for radial and mixed turbines for the compressible case. Today his method is still often used for designing radial turbine machinery. Zhu et al. performed inverse design optimization of the reversible pump-turbine [11], while also considering cavitation characteristics. Leguizamón and Avellan [12] very recently provided an open-source implementation of an inverse Francis turbine design, together with a validation study confirming the approach's appropriateness. Cavitation is not often studied using inverse design methods; among the available studies, Daneshkahi and Zangeneh [13] linked the blade loading and blade stacking to the efficiency and cavitation characteristics of a Francis runner, providing a valuable physical understanding and useful design guidelines.

The 3D design of the runners and the guide apparatus may be determined by performing consecutive CFD calculations, while constantly varying 3D geometry and design parameters [9,14]. Unfortunately, CFD alone is unable to establish an optimized 3D design. A 3D design study using CFD was performed by Xue et al. [15], considering the efficiency, stability of design, and cavitation of a pump turbine during pumping mode. A comprehensive hydraulic and parametric analysis of a Francis turbine runner was performed by Ma et al. [16]. They [16] performed a multipoint and multiobjective optimization design procedure, achieving efficiency improvements up to 0.91%. The optimization procedure included the 3D inverse design method, CFD analysis, and multipoint and multiobjective optimization technology.

Runner blades are central turbine elements, where energy is transferred from the fluid to the generator shaft. Blade sizes and angles, including hydrofoil selection, contribute to the blade design. The blade design is often a trade-off between efficiency, cavitation development, and cavitation erosion. A pressure difference between the suction and pressure sides is limited by cavitation, while at the same time the high pressure difference enables energy transfer from water to the generator. If the turbine is at full load and the water level is low in the reservoir, the pressure on the suction side may decrease and locally drop below the vapor pressure. Cavitation on the runner blades may appear in several locations. These are the turbine blade leading edge, the tip, the pivot, the gap between the blade tip and the discharge ring, the blade suction side close to the trailing edge, and the cavitation near the draft tube cone [7,17]. For the abovementioned cavitation types, the root causes are suboptimal runner blade design and hydrofoil selection for the selected operating conditions. Cavitation is extensively studied in hydraulic turbine machinery; among these, few studies have employed the visualization method [6,7].

On bulb turbines' blades, the initial cavitation most often appears at the location with the highest local speed i.e., at the blade tip [18]. We show an experimental analysis of a modification to the hydrofoil design of bulb turbine blades so as to resist cavitation during continuous operating conditions at high flows. The paper shows the cavitation characteristics of two bulb turbine hydrofoils. The improvement from the existing to modified hydrofoil is discussed based on visualization analysis in the cavitation channel. Furthermore, we show a comparison of the modified runner blades with the unmodified blades in terms of the turbine output. The paper shows marked improvement in cavitation occurrence between existing and modified hydrofoils, and a confirmed regression model of the void fraction.

2. Hydrofoil

Bulb turbine (Figure 1) blade hydrofoils are optimized for a mix of parameters, among which are maximum hydraulic efficiency, high output power, minimum turbine vibrations, high strength, reduced fatigue, and reduced cavitation phenomena. Reduced cavitation enables operators to reduce the service intervals required for cavitation damage repair and welding costs, as well as loss of money for nonoperation.

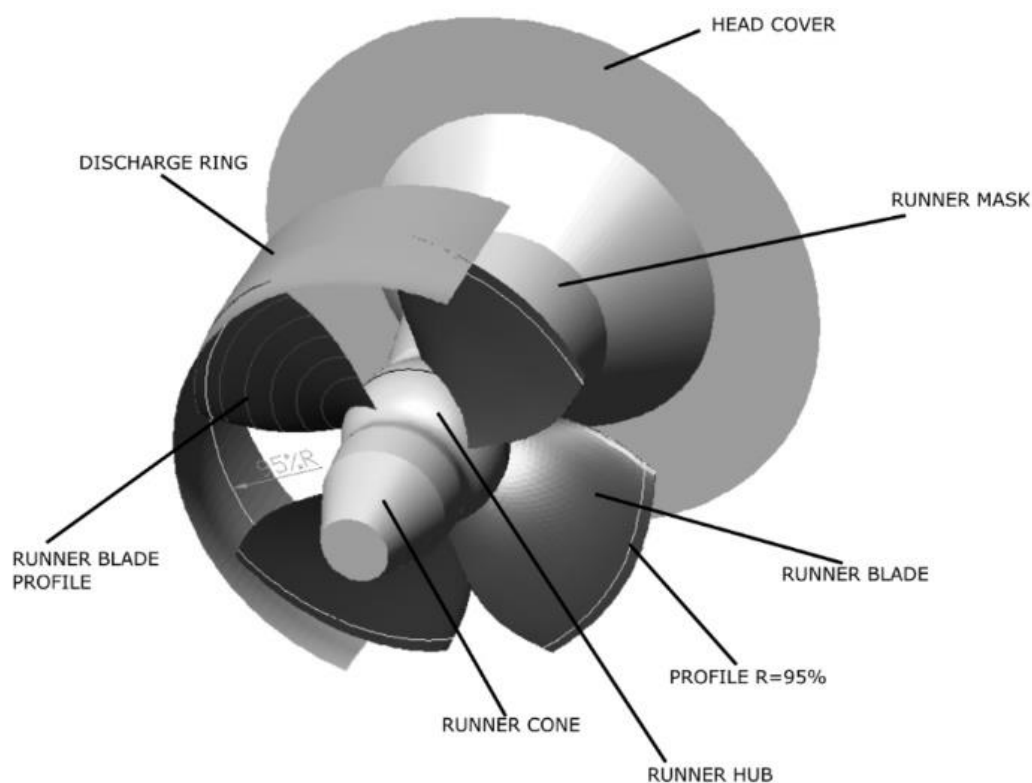


Figure 1. Bulb turbine runner.

In this study, we focus on a range of volumetric flows, which appear on a bulb turbine at a 25° blade angle (Figure 2). Here cavitation frequently occurs at approximately 15% higher volumetric flows than at the best efficiency point [6]. The 25° blade angle was chosen because it lies in the middle of the angle interval usually agreed between the producers and customers of bulb turbines. The blade angle 25° is often reinforced during performance or acceptance tests [18], because it corresponds to both common operating conditions and features increased probability for cavitation.

The bulb runner blade hydrofoil's shape determines the flow conditions in the runner. Well-shaped 3D blade hydrofoils reduce the inception and the growth of cavitation on the bulb turbine runner hydrofoils. Turbine hydrofoil profiles were used in designing the bulb runner blade's 3D shape, spanning from the runner hub toward the blade tip (Figure 2). For reliable 3D characterization of the turbine runner blade, and thus the entire bulb runner, several hydrofoils are usually selected. Later, a smooth surface is drawn over all hydrofoils to form the entire 3D geometry of the runner blade, further enabling CFD or experimental analysis.

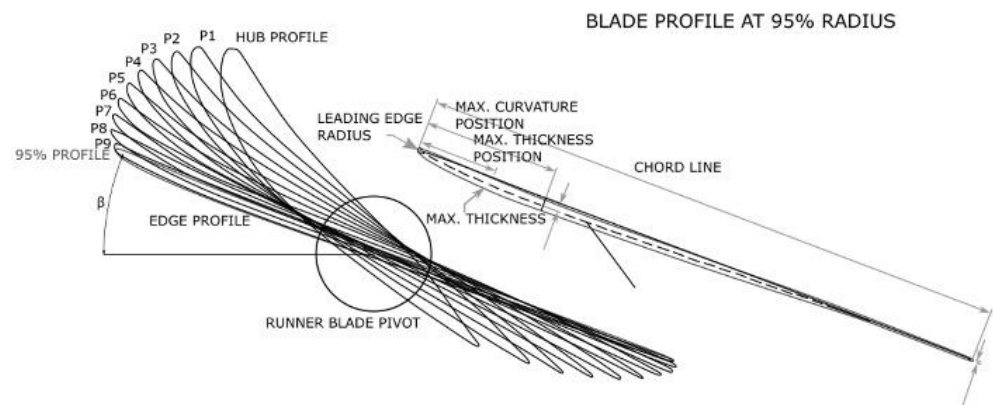


Figure 2. Selection of a 25° angle on a modified bulb turbine hydrofoil.

Although the bulb turbine blade can consist of many hydrofoils as explained above, in this paper we focus on a single hydrofoil. The most potential for energy conversion in bulb turbines is available near the tip, where tangential blade velocity and flow velocities are high. Due to high velocities, large pressure gradients, and the vicinity of the tip gap flow, this region is highly susceptible to cavitation occurrence and surface erosion. Here, several cavitation structures are usually found during acceptance tests. To focus on the cavitation properties of the hydrofoils, we have selected for further analysis the hydrofoil at 95% bulb turbine diameter D , measured from the runner rotation axis to the blade tip. The selected hydrofoil is thus located near the tip as shown in Figures 2 and 3. We made this selection on the basis of the energy transfer. Most of the energy is transferred where the turbine blade has a large diameter and the blade has a high surface area, and where the blade and flow velocities are high.

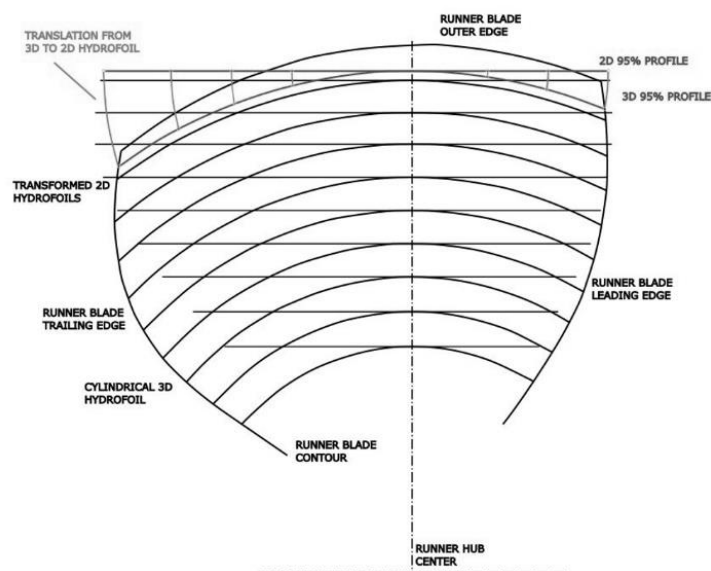


Figure 3. Bulb turbine blade design from individual 2D hydrofoils.

Hydrofoils have been studied extensively, including profile families such as NACA (among them 4–8 series), Göttingen, Munk, NPL, and others [19–21]. The available families of hydrofoils facilitate the turbine engineer's selection of the blade's hydrofoil to suit the required operating intervals and conditions, inter alia, for operation at high volumetric flows and runner blade angles. To enable operation in specific operating conditions, including cavitation properties, the turbine designer selects hydrofoil properties like leading

edge radius, camber, location of maximum thickness, maximum curvature, and trailing edge design.

The locations of cavitation occurrence on bulb turbine blades are well documented in [22]. In the hill diagram, we will focus on the high discharge region. Here, the cavitation is found in four regions [22]: the blade suction side, blade pressure side, fillet, and tip gap. The flow properties in and near the gap are dominated by turbulence and may appear in the entire hill diagram. The hydrofoil properties that most affect the cavitation on the blade suction and pressure side are the leading edge radius, the location of maximum thickness, and the curvature; we may also assume that the blade angle in bulb turbines is always optimal due to the turbine's dual regulation. We want to design a leading edge such that the flow around it is smooth so as to prevent any flow separation. As discussed above, we will focus on the hydrofoil at 95% of the blade radius, where we assume that in addition to the mentioned leading edge, maximum thickness and curvature influence, the cavitation properties are also influenced also by the presence of the gap flow. At 95% of the blade radius, the flow properties (velocity and pressure) are more pronounced because of higher blade velocity than near the hub. The sharp leading edges may introduce flow separation [23] and deteriorate the flow properties further downstream from the leading edge. Downstream from the leading edge the flow is determined by the camber shape, the position of maximum curvature, maximum thickness, etc. These parameters, among others, determine the velocity distribution in the blade channel from the pressure to the suction side. Velocity is related to absolute pressure; an increase in flow velocity decreases the local pressure [7], thus, the velocity distribution affects the cavitation properties. The pressure distribution may cause local cavitation inception, and both can influence boundary layer separation.

The hydrofoils in the bulb or any other water turbines are the base elements of the turbine runner blades and are thus rotating. The bulb turbine features pressure distribution with the pressure normally decreasing from the leading edge towards the trailing edge. According to the bulb turbine's triangles of velocity, downstream from the hydrofoil the relative velocity increases and reaches its maximum near the trailing edge [7], and the situation is remarkably different in comparison with the single hydrofoil in the water tunnel. Furthermore, the pressure distribution around the hydrofoil in the cavitation tunnel cannot fully represent the pressure properties around the bulb turbine blade. The situation in the bulb turbines is therefore very complex and the flow properties around individual hydrofoils cannot be directly correlated around the bulb turbine runner blades. Nevertheless, we will assume [6] that bulb runner cavitation can be related to the cavitation analysis of a single hydrofoil in the water tunnel.

Hydrofoil Modifications

The turbine blade hydrofoils are the primary component of the turbine blades. To improve performance, the turbine hydrofoil profiles should be smoothly and consistently remodelled in a spatial 3D redesign of the entire bulb turbine runner blade. The new blade differs from the old in the following parameters: the leading-edge radius has increased, the maximum thickness location has moved forward, and the location of the maximum hydrofoil curvature has moved forward. The characteristics of both turbine hydrofoils are shown in Table 1.

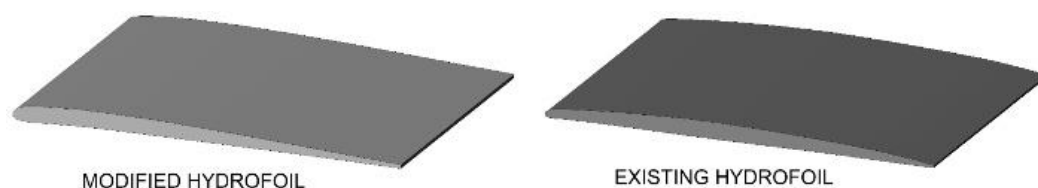
Table 1. Characteristics of hydrofoils as used on bulb turbine.

Parameter	Modified	Unmodified
Runner diameter D_0	\varnothing 350 mm	\varnothing 350 mm
Number of runner blades Z	4	4
Location of reference hydrofoil R_h	95% D_0	95% D_0
Blade angle β_0	25°	25°
Blade chord line length at 95% R	180.7 mm	180.7 mm
Location of maximum thickness l_1	27.11 mm	72.28 mm
Ratio l_1/l	15%	40%
Location of maximum curvature l_2	54.2 mm	81.3 mm
Ratio l_2/l	30%	45%
Leading edge radius r_0	1.63 mm	1.27 mm

The modified hydrofoil as compared to the unmodified one features reduced absolute velocity in a section from the location of the maximum hydrofoil thickness and curvature to the trailing edge. The cavitation properties of the modified hydrofoil as compared to the unmodified one are in this section favorable. Because the points of maximum thickness and curvature for the modified hydrofoil profile were moved forward towards the leading edge, this section is relatively long.

The unmodified hydrofoil in a region from the leading edge to the location of the maximum thickness is very sensitive to the optimum angle of attack due to its sharp leading edge. Away from the optimum attack angle, the unmodified hydrofoil has disadvantageous cavitation characteristics in comparison with the modified one [6]. Contemporary water turbines often operate away from the best efficiency points due to the introduction of renewable energy sources and environmental changes. This trend will most probably increase in the future.

Two dimensional hydrofoils (Figure 4) were created from the 3D spatial bulb turbine blade hydrofoils (Figures 2 and 3). The 3D turbine blade hydrofoil was transformed from the cylindrical coordinate system of a turbine blade to a planar Cartesian x - y coordinate system as shown in Figure 3.

**Figure 4.** Hydrofoils used in the cavitation tunnel analysis.

As shown previously, both hydrofoils correspond to the runner blades' profiles at 95% R (Figure 3). The properties of both bulb runners are given in [4]. The turbine runners and both 2D hydrofoils were manufactured from brass using the same manufacturing techniques and both were given the same surface processing. The hydrofoils were later subjected to flow and image analysis in a cavitation tunnel and regression modelling.

The hydrofoil parameters for the experiment in the cavitation tunnel are shown in Table 2. The same manufacturing method as for the hydrofoils on the bulb turbine was used for the manufacture of the hydrofoils used in the cavitation tunnel.

Table 2. Hydrofoil parameters.

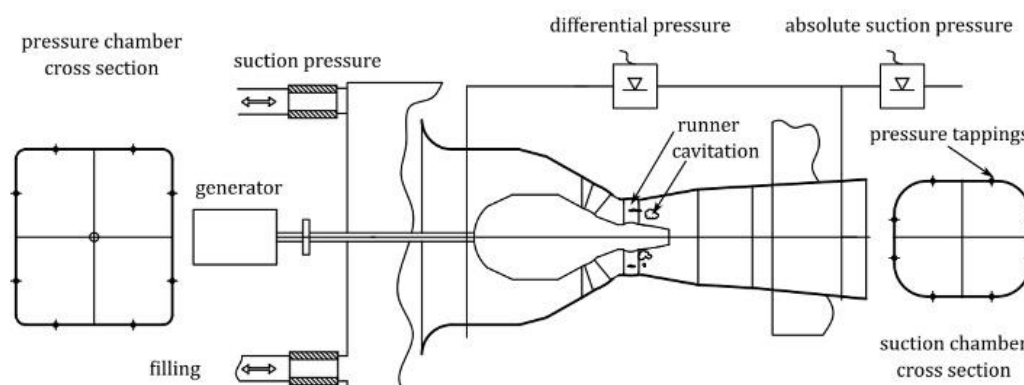
Parameter	Modified Hydrofoil	Existing Hydrofoil
Hydrofoil chord length l	60 mm	60 mm
Maximum hydrofoil thickness d_{\max}	2.55 mm	2.55 mm
Maximum thickness position l_1	9 mm	24 mm
Maximum thickness position ratio l_1/l	15%	40%
Maximum hydrofoil curvature s_{\max}	0.87 mm	0.87 mm
Maximum curvature position l_2	18 mm	27 mm
Maximum curvature position ratio l_2/l	30%	45%
Radius at the Leading edge r_0	0.54 mm	0.42 mm

3. Experiment

Experiments were performed on the turbine measuring station for both bulb turbine runners and in the cavitation tunnel for both hydrofoils. A turbine measuring station was used to determine efficiency for a single runner blade angle. In the cavitation tunnel, cavitation properties were measured for analogous operating points.

3.1. Turbine Measurements

Measurements of efficiency were performed on a low-head axial and bulb turbines measuring station for low-head bulb turbines (Figure 5) in Kolektor Turboinštitut (Ljubljana, Slovenia). The measuring station was built according to standard [18] and was used for the model, witness, and acceptance tests. In agreement with standard [18], all measurements and data acquisitions were automatic. The nominal runner diameter of the test rig is 350 mm, and the recirculating flow is generated using two radial pumps with frequency regulation. The flow measurement was performed by using an electromagnetic flowmeter with a diameter of DN 400 and an accuracy of $\pm 0.15\%$. The static pressure was measured using a differential pressure transducer (accuracy of $\pm 0.025\%$), with the measuring taps located on the inlet and the outlet. Absolute suction pressure was measured using an absolute pressure transducer with an accuracy of $\pm 0.025\%$ to assure that the measuring station operated well above the incipient cavitation number. An electromagnetic incremental sensor was used to measure the rotational speed; the output was processed by a counter-timer module with an accuracy of $\pm 0.01\%$. The shaft torque was measured on a horizontal shaft using a rotating torque transducer with an accuracy of $\pm 0.01\%$. The friction torque was estimated by operation with air.

**Figure 5.** Turbine measuring station.

Both bulb turbine runners were tested under similar conditions at six operating points. The blade angle was cases set to 25° in all cases (Figure 6). The blade angle was set using a control template. For comparison, both runners operated at the same specific energy E (J/kg) and the corresponding nondimensional energy numbers ψ were recorded. E was

determined from the total specific energy at the turbine inlet and the outlet cross-sections [7]. Energy numbers ψ were determined using the equation:

$$\psi = \frac{2 \cdot E}{\pi^2 \cdot N^2 \cdot D^2} \tag{1}$$

Here N (min^{-1}) is the rotational frequency, while D (m) is the discharge ring diameter of the bulb turbine. The turbine rotational frequency N (1000 min^{-1}) was the same for all measuring points. Both runners had the same nominal diameter D (m). The guide vane opening coefficient A_0 was the same for each pair of measuring points used in the comparison:

$$A_0 = \frac{a_v \cdot z}{D_v} \tag{2}$$

a_v (mm) is the guide vane’s opening and z (/) is the number of guide vanes. D_v (mm) is the guide vane pivot diameter. Important manufacturing methods and characteristics were kept the same for reliable comparison between both runners. Control of runner tip gaps to the discharge ring and clearances of guide vanes to the guide vane pressure rings are very important for reliably estimating model turbine runners. Both runners were manufactured from the same material and using the same production methods and procedures. As such, for both runners, the tip gaps, guide vane clearances, and surface finishes were the same.

The measuring station was of a closed type. To maintain the ψ fixed, the main water circulation pump’s frequency was controlled. The volumetric flow Q (m^3/s) represented in its nondimensional form as flow number φ [18] is:

$$\varphi = \frac{Q}{\pi^2 / 4 \cdot N \cdot D^3} \tag{3}$$

The results from a previous study show that the increase in efficiency amounts to around 1% for the same runner geometry. Most of the increase according to the hill diagram is due to the small shift of the operating points towards low flow numbers and higher efficiency [6].

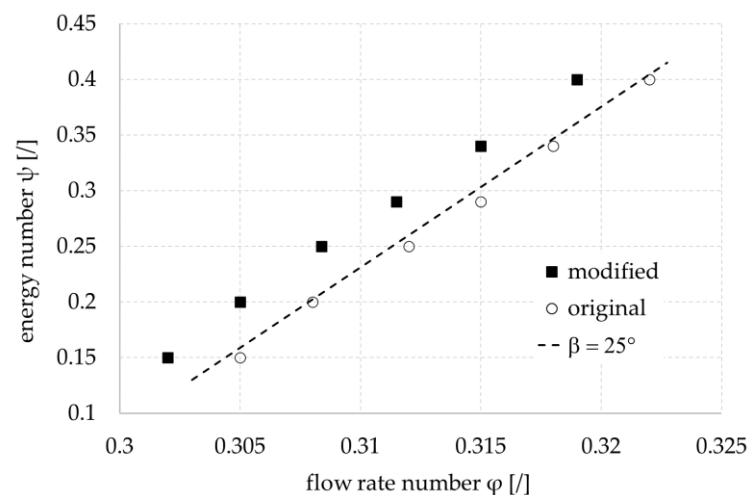


Figure 6. Turbine measuring points.

3.2. Cavitation Tunnel Measurements

The flow visualization measurements were taken on the cavitation measuring station. The approach to investigating the turbine blade flow properties in a separate tunnel experiment was similar to that used in [24]. A closed-type cavitation measuring station was used as shown in Figure 7. The flow was provided by a centrifugal pump driven

by a frequency variable drive. The volumetric flow measurement was performed using an electromagnetic transducer ABB COPA-XL. Absolute pressure p_{abs} was measured on the suction side using an ABB 2600T 264NS pressure transducer. The temperature was measured by a Pt-100 4 wire temperature transducer, connected to the Agilent 34970A data acquisition unit. Valves in front of and behind the test section were fully open during experiments and they were only used during installation. Suction pressure was set using a vacuum pump, located on the top of a tank with a free water surface.

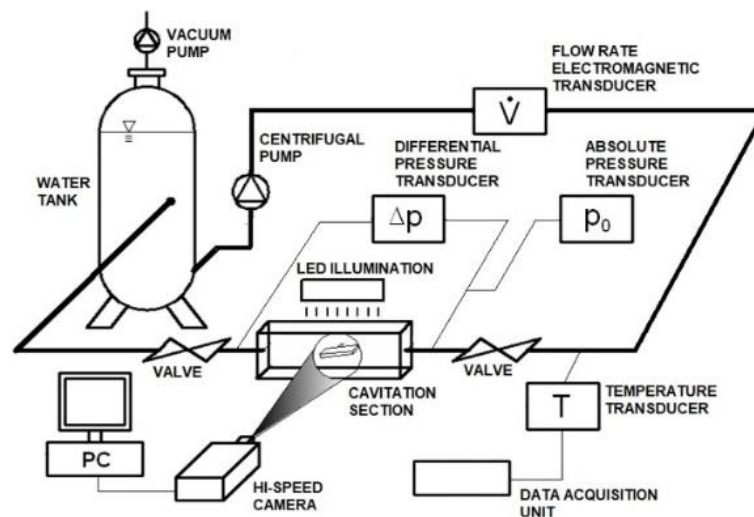


Figure 7. Cavitation measuring station with measuring and visualization equipment.

The cavitation tunnel test section cross-section was $50 \text{ cm} \times 100 \text{ cm}$. Hydrofoil width was 50 mm and chord length was $l = 60 \text{ mm}$. The hydrofoil was installed at the angle of attack 8° .

A high-speed Photron SA-Z camera was used together with a Nikkor 105 mm 1:2.8 lens to visualize the cavitation in the cavitation section. The camera was mounted from the side. The camera was operated in a free-running mode. Images were recorded using PFV software in 8-bit BMP black and white mode at a resolution of 640×280 . The framerate used was 25,000 frames/s. Shutter speed was equal to $10 \mu\text{s}$. For each operating point, 2000 frames were recorded. For all experiments, all other camera settings were the same. A high intensity continuous LED illumination was provided by many CREE XLamp XM-L LED modules. LED modules were powered by an Instek DC power supply. Illumination was provided from the top of the test section above the hydrofoil on its suction side and arranged such that as few reflections as possible were present in the recorded sequences. Illumination intensity was not the same for all experiments; with the modified hydrofoil it was necessary to increase illumination intensity to visualize weaker cavitation structures. Keeping the illumination constant was impossible due to the low 8-bit depth of recorded images.

We have selected two dimensionless numbers to describe the cavitation in the cavitation tunnel, namely the Reynolds number Re and cavitation number σ . In Reynolds number Re

$$Re = \frac{L \cdot v}{\nu} \quad (4)$$

L is hydrofoil length, v (m/s) is flow velocity in front of the hydrofoil and ν is the kinematic viscosity of water. To obtain the hydrofoil cavitation characteristics, the cavitation numbers σ were evaluated. Cavitation number σ was calculated according

$$\sigma = \frac{p_{abs} - p_v}{\rho \cdot v^2} \quad (5)$$

where p_v (N/m^2) is the water evaporation pressure and p_{abs} (N/m^2) is absolute pressure. Water evaporation pressure was estimate using the Equation

$$p_v = 10^{2.7862+0.0312 \cdot T_w - 0.000104 \cdot T_w^2} \quad (6)$$

where T_w ($^{\circ}C$) is water temperature. Equation (6) provides for a maximum difference of 0.2%, with a negligible influence on the measurements.

The cavitation σ - η curve is used to estimate the cavitation properties of bulb turbines. The cavitation point for the highest cavitation numbers is measured at ambient pressure, while for subsequent cavitation points suction pressure is decreased. For the tunnel measurements the cavitation number σ was used to observe the cavitation's development on both hydrofoils. For each experiment, the absolute pressure p_{abs} was set as constant at the inlet of the cavitation tunnel. To decrease the cavitation number σ we increased the flow Q (m^3/s) and flow velocity. Several such operating points were measured for increasingly lower absolute pressure p_{abs} in the test section. This enabled comparison between both hydrofoils and among different absolute pressures.

The measuring points for both hydrofoils were selected according to cavitation structures sizes, shapes, and intensities. In general, cavitation intensity increased as cavitation number σ decreased. Instantaneous cavitation numbers σ were selected manually; we wanted to capture significant visible structural changes in cavitation. Such a procedure captured all important structures, starting with incipient cavitation on the leading edge, then sheet cavitation, cloud cavitation, and supercavitation across the entire hydrofoil [25,26]. Cavitation structure formation on both hydrofoils emerged at different cavitation numbers σ and, thus, the selection of cavitation number σ and corresponding measuring points for both hydrofoils was not the same.

3.3. Cavitation Image Analysis

Illuminated cavitation structures on the hydrofoils were recorded in a set of black and white images using the experimental setup from Section 3.2. The cavitation structures in the image have elevated grey level intensities, with vapor phase forming time and 2D space-dependent structures [22,27]. With computer-aided visualization of the process, the simultaneous time series of images were recorded. An assumption was made that the intensity of the illumination is proportional to the amount and intensity of the void fraction, being further proportional to the intensity of the cavitation structures in the observed regions [23]. This assumption is credible for cavitation intensity, low void fractions, and corresponding ratios of the intensity of the void fraction and grey level.

The time series of images from high-speed visualization in the cavitation tunnel were analyzed such that individual traveling bubbles were first filtered out. All bright objects in the individual image were deleted whenever they were very small. All other objects, like the attached cavitation or cavitation clouds, were retained. From these filtered images, the average grey level $E_g(i,j,t)$ and standard deviation were calculated as explained below.

The grey level variable $E_g(i,j,t)$ was acquired by processing intervals of 256 grey levels (8-bit camera image depth) from black (intensity = 0) to white (intensity = 255). The averaged grey level series were calculated in observation region. The standard deviation was estimated using the equation below:

$$S(i,j) = \sqrt{\frac{1}{T} \sum_{t=1}^T [E(i,j,t) - \langle E_g(i,j) \rangle]^2} \quad (7)$$

Here $\langle E_g(i,j) \rangle$ is time and spatially averaged grey level, which is proportional to the average void fraction of the cavitation structure's.

$$\langle E_g(i,j) \rangle = \frac{1}{T} \sum_{t=1}^T E(i,j,t) \quad (8)$$

The time interval t in Equations (7) and (8) is set from the duration and frequency of acquisition.

A sample of image analysis is shown in Figure 8 for the existing hydrofoil ($p = 0.15$ bar; $Q = 61.7$ m³/h; $\sigma = 2.27$) and in Figure 9 for the modified hydrofoil ($p = 0.15$ bar; $Q = 61.7$ m³/h; $\sigma = 2.27$). Cavitation length for the selected operating points was estimated to $L = 22.74$ mm for existing hydrofoil and $L = 11.27$ mm for modified hydrofoil. Such a method of estimating cavitation length was used for all operating points for both hydrofoils and later for regression cavitation length modelling.

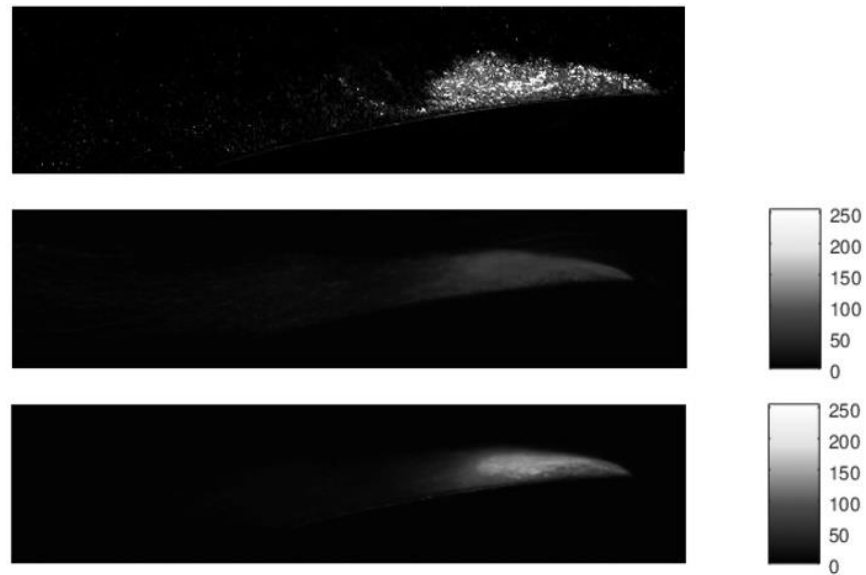


Figure 8. Original hydrofoil, a sample image of cavitation (**top**), spatially averaged grey level (**middle**), and standard deviation of grey level (**bottom**), operating point $p = 0.15$ bar, $Q = 61.7$ m³/h, and $\sigma = 2.27$.

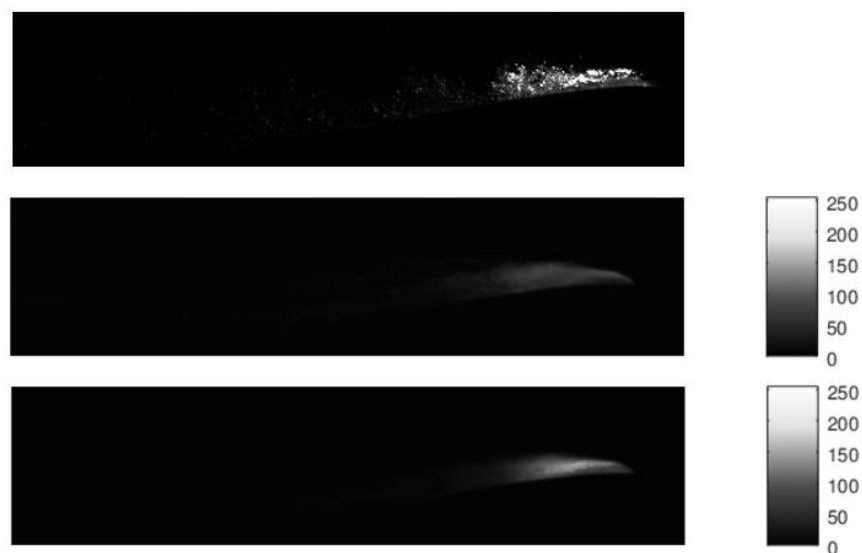


Figure 9. Modified hydrofoil, a sample image of cavitation (**top**), spatially averaged grey level (**middle**), and standard deviation of grey level (**bottom**), operating point $p = 0.15$ bar, $Q = 61.7$ m³/h, and $\sigma = 2.27$.

3.4. Regression Cavitation Length Model

Cavitation properties are a consequence of flow parameters, which are best described using Reynolds number Re and cavitation number σ . We will show that cavitation length on a hydrofoil in a cavitation tunnel may be well predicted based on these two dimensionless numbers. A good correlation is expected between the measured and calculated cavitation lengths. For this, we will use the following power-law regression model for cavitation length L

$$L = \beta_0 \cdot Re^{\beta_1} \cdot \sigma^{\beta_2} \quad (9)$$

Model parameters β_0 , β_1 , and β_2 were calculated using the minimum mean square error method.

4. Results and Discussion

We have shown in Figure 6, that two bulb turbine runners with differently shaped blade hydrofoils (Figure 4) show very similar pressure characteristics. Because both runners are different, their hill diagrams and characteristics, in general, cannot be compared. The analysis of the cavitation properties of both hydrofoils will be shown in the following section. As an attempt to provide the background for the bulb runner evaluation with a focus on cavitation, two differently shaped hydrofoils were tested in the cavitation channel. We observed cavitation phenomena as a result of the hydrofoil shape design. The main tool for analyzing the cavitation structures appearing on the hydrofoil surface was computer-aided visualization. From these cavitation images, the cavitation length was measured and used to make the regression model.

4.1. Cavitation Dependence on the Cavitation Number σ

The visual comparison and analysis of the two hydrofoils as a direct result of decreasing cavitation number σ is shown in Figures 10–13. Cavitation numbers from high to low were selected such that a marked difference in cavitation structures occurrence was observed. The selected images represent to the greatest extent possible the most typical conditions for selected cavitation number σ . The analysis was limited to the hydrofoil suction side. A decrease in the cavitation number increases the intensity and amount of the cavitation structures. We will demonstrate that shape modification is essential for cavitation to occur on hydrofoils. A modified hydrofoil will demonstrate a decrease in cavitation phenomena intensity in comparison to an existing hydrofoil. The main area of visualization is over the hydrofoil’s leading edge and the entire suction side of the hydrofoil.

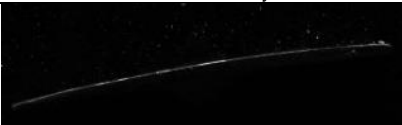
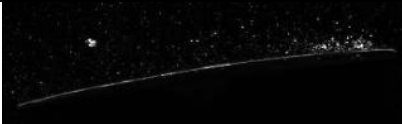
Existing Hydrofoil	Modified Hydrofoil
Cavitation number $\sigma = 4.85$; Reynolds number $Re = 269,571$	
	
Cavitation number $\sigma = 4.45$; Reynolds number $Re = 281,340$	
	
Cavitation number $\sigma = 4.1$; Reynolds number $Re = 293,635$	
	
Cavitation number $\sigma = 3.65$; Reynolds number $Re = 311,201$	

Figure 10. Cont.

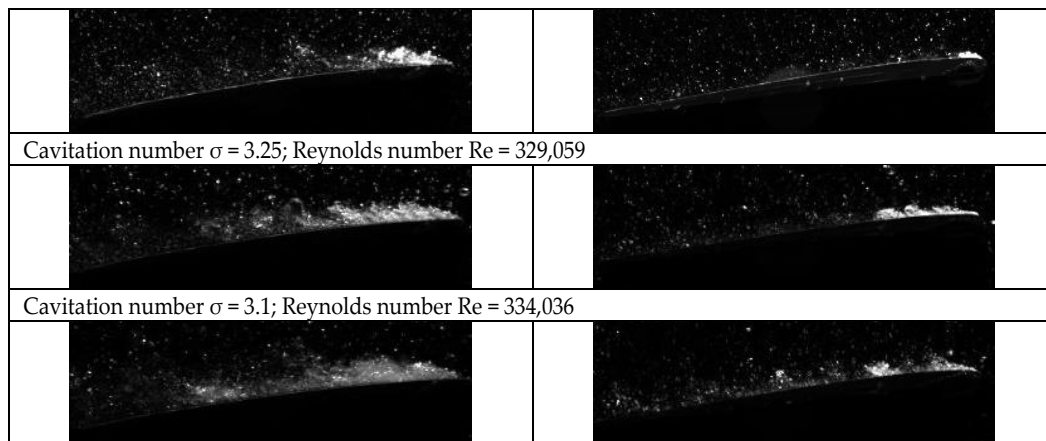


Figure 10. Visualization results of cavitation structures at $p_{abs} = 0.65$ bar.

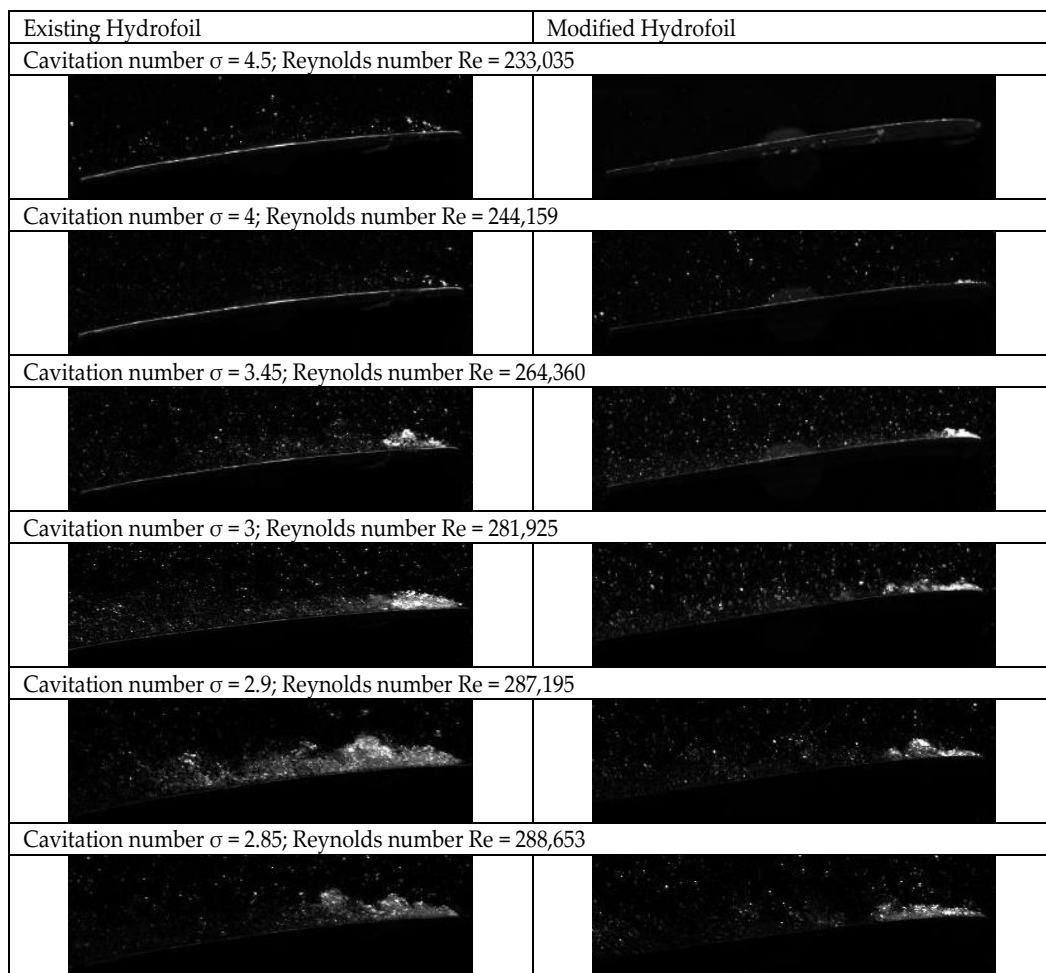


Figure 11. Visualization results of cavitation structures at $p_{abs} = 0.45$ bar.

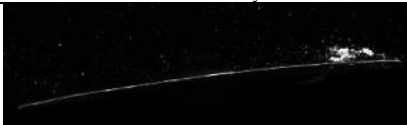
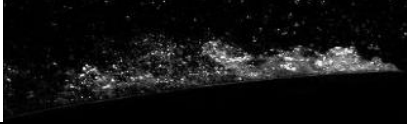
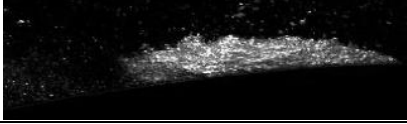
Existing Hydrofoil	Modified Hydrofoil
Cavitation number $\sigma = 3.55$; Reynolds number $Re = 209,907$	
	
Cavitation number $\sigma = 3$; Reynolds number $Re = 230,400$	
	
Cavitation number $\sigma = 2.6$; Reynolds number $Re = 246,502$	
	
Cavitation number $\sigma = 2.55$; Reynolds number $Re = 249,722$	
	
Cavitation number $\sigma = 2.4$; Reynolds number $Re = 255,284$	
	

Figure 12. Visualization results of cavitation structures at $p_{abs} = 0.30$ bar.

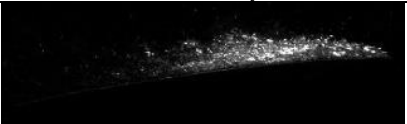
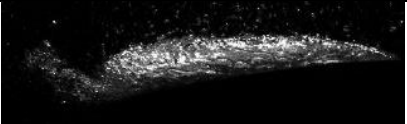
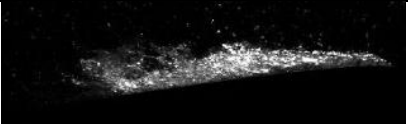
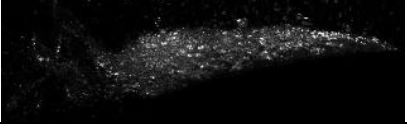
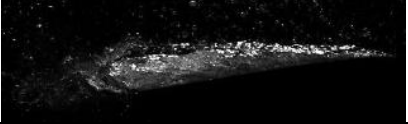
Existing Hydrofoil	Modified Hydrofoil
Cavitation number $\sigma = 2.85$; Reynolds number $Re = 161,895$	
	
Cavitation number $\sigma = 2.25$; Reynolds number $Re = 180,631$	
	
Cavitation number $\sigma = 1.82$; Reynolds number $Re = 200,831$	
	
Cavitation number $\sigma = 1.45$; Reynolds number $Re = 225,130$	
	
Cavitation number $\sigma = 1.4$; Reynolds number $Re = 228,936$	
	

Figure 13. Visualization results of cavitation structures at $p_{abs} = 0.15$ bar.

Figures 10–13 are limited to the intervals of the cavitation number that we were able to achieve in the cavitation tunnel with relevant cavitation intensities.

The measurements at absolute pressure $p_{\text{abs}} = 0.65$ bar are shown in Figure 10. Cavitation structures (void fraction) start to appear on the modified hydrofoil at cavitation number around $\sigma = 3.65$. The cavitation starts behind the leading edge as an attached cavitation. With the further decrease of the cavitation number to around $\sigma = 3.1$ we observed an increase in the cavitation intensity and the quasiperiodic shedding of cavitation clouds. On the other hand, cavitation was observed on the original hydrofoil at cavitation numbers around $\sigma = 4.45$. At cavitation number $\sigma = 3.65$ we observed some cavitation cloud shedding, and at cavitation $\sigma = 3.1$ more than two-thirds of the hydrofoil was cavitating. At cavitation $\sigma = 3.1$, with the modified hydrofoil, the cavitation length was only 1/3 of the hydrofoil length. Since the hydrofoils in both cases were attached at the same angle of attack, we assume that the difference in cavitation occurrence is due to the shape and curvature of the leading edge. A sharp leading edge cuts through the flow such that it cannot follow the hydrofoil shape immediately downstream from the leading edge. The resulting flow separation induces cavitation inception due to the low absolute pressure and high velocity.

The measurements at absolute pressure $p_{\text{abs}} = 0.45$ bar are shown in Figure 11. The cavitation on the modified hydrofoil profile starts behind the leading edge as an attached cavitation around $\sigma = 3.45$, and $p_{\text{abs}} = 0.65$ bar. At cavitation $\sigma = 3$ we again observed cavitation cloud shedding as in Figure 10. The cavitation is much more intense for the case of the existing hydrofoil. We observed cavitation inception already at around $\sigma = 4.5$, while almost the entire hydrofoil was cavitating around $\sigma = 3$.

The measurements at the absolute pressure $p_{\text{abs}} = 0.30$ bar are shown in Figure 12. Measurements commenced around $\sigma = 3.55$; at this operating point the incipient cavitation is already present. Incipient cavitation here is present as an attached cavitation. For the modified hydrofoil, the attached cavitation formed only at around $\sigma = 3$; it covered up to around half of the hydrofoil length. With the original hydrofoil, the cavitation inception began around the same cavitation number ($\sigma = 3.55$) as for the modified hydrofoil, although with slightly higher intensity. A remarkable difference in the intensity of cavitation was observed at cavitation number $\sigma = 3.0$. Here, the cavitation cloud is much larger for the existing hydrofoil. Below the cavitation number $\sigma = 2.6$ most of the hydrofoil is covered by a thick cavitation cloud in the case of the existing hydrofoil.

The measurements at absolute pressure $p_{\text{abs}} = 0.15$ bar are shown in Figure 13. With modified hydrofoil, no cavitation was observed around cavitation number $\sigma = 2.85$, while with the original hydrofoil the cavitation cloud at around $\sigma = 2.25$ covers up to one-third of the hydrofoil length. At around $\sigma = 1.82$ the cavitation cloud is again more intense than at cavitation number $\sigma = 2.25$. Below around cavitation number $\sigma = 1.45$ both hydrofoils are fully covered with supercavitation.

At cavitation numbers below around $\sigma = 1.82$ the large cavitation structures reduce the water passage area and increase the flow velocity in the cavitation tunnel at the selected flow. The results show favorable cavitation characteristics for the modified hydrofoil in comparison with the unmodified hydrofoil. We may also assume that the runner blade designed from such hydrofoils can perform well in the bulb turbine when operating under cavitation conditions.

4.2. Cavitation Length Model

Among several possible parameters of the cavitation flow properties, we have selected the cavitation cloud length for regression modelling. The results of the cavitation length model are shown in Table 3. Cavitation length dependence on the parameter β_0 is modest at around 6% in favor of existing hydrofoil. The modified hydrofoil's dependence on the parameter β_1 shows that the cavitation length of the modified hydrofoil is lower than that of the existing one. The most important improvement of the modified hydrofoil over the existing one is hidden in the dependence on cavitation number σ (achieving a value at

parameter β_2 of -3.4 , improving over the original -2.93). The results of the cavitation length model confirm the modified hydrofoil’s superior cavitation characteristics over the existing one.

Table 3. Cavitation length model parameters for modelled cavitation length L.

	Parameter		
	β_0	β_1	β_2
Existing hydrofoil	2.81×10^{-8}	1.88	-2.93
Modified hydrofoil	2.99×10^{-8}	1.86	-3.40

The regression diagrams of the measured and modelled cavitation lengths are shown in Figures 14 and 15. The coefficients of determination for both the existing and modified hydrofoil profiles are reasonably good, with values above $R^2 > 0.95$. The high values of both coefficients of determination confirm the validity of the cavitation length model.

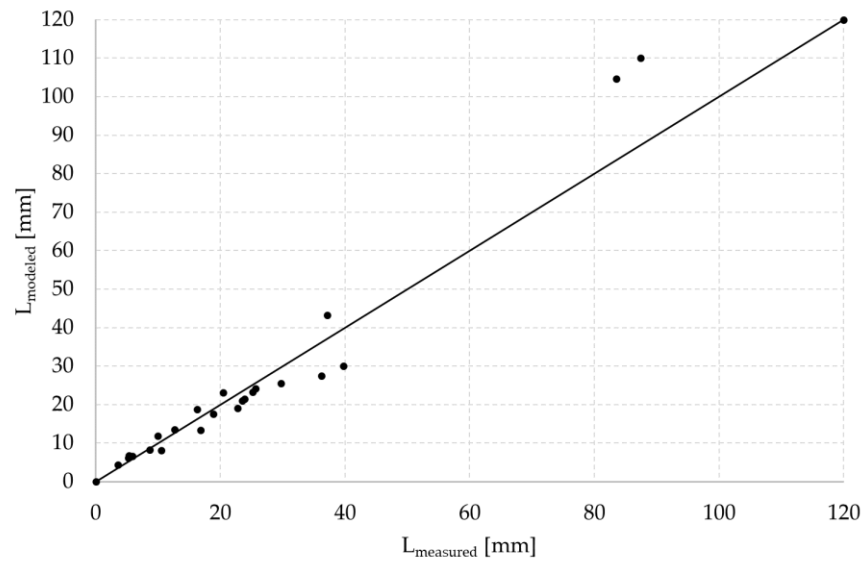


Figure 14. Cavitation model for existing hydrofoil, coefficient of determination $R^2 = 0.9586$.

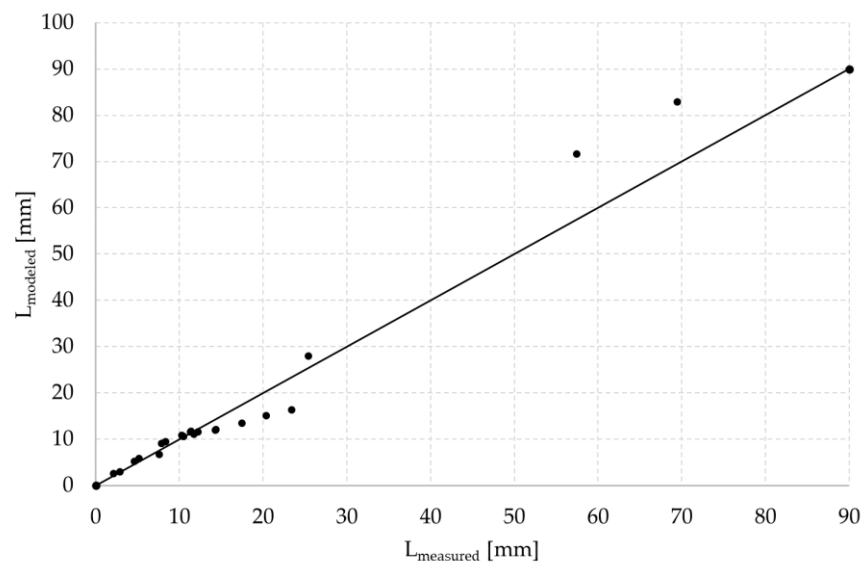


Figure 15. Cavitation model for the modified hydrofoil, coefficient of determination $R^2 = 0.9858$.

5. Conclusions

In future power grids, waterpower flexibility will be an important parameter for ensuring network stability. Water turbines will need to operate at wide flow intervals and in transient regimes, and also allow for fast response times. For this reason, among others, further research on cavitation is required.

The goal of this research was to demonstrate the relation between the hydrofoil shape and cavitation phenomena. Existing and modified hydrofoils were extracted from runner blades on the 95% runner blade radius and modified. The modifications were made on the hydrofoil's leading edge, as well as at the points of maximum thickness and curvature. The leading-edge radius was enlarged to avoid flow separation. Maximum thickness and curvature were moved in the direction of the leading edge to stabilize the flow around the hydrofoil towards the trailing edge. Both hydrofoils were implemented in a bulb turbine and measured under equal energy numbers. Measurements of both turbine runners were performed on the measuring station according to the standard for acceptance tests of water turbines.

The results of this study show improved cavitation characteristics. However, we show here only a single modification of the hydrofoil and the results only demonstrate the efficiency of this modification. Of particular benefit for future design would be a comprehensive study, providing for a hydrofoil and runner shape optimization algorithm, based on selection and later minimization of the objective functions, including the manufacture and measurements of a selection of hydrofoils and runners.

To evaluate the cavitation properties, the flow was visualized in the cavitation tunnel on the suction side. The modified hydrofoil exhibited improved cavitation properties and we chose to evaluate the intensity of the cavitation using the cavitation cloud length. A regression model prediction of the cavitation length shows that modified hydrofoil features improved cavitation characteristics in comparison with the existing hydrofoil.

The primary goal of this study was to provide for improved cavitation characteristics on the modified hydrofoil. Using the modified hydrofoil invariably changes runner characteristics and this resulted in operating points shifting to the left in the hill diagram. This leftward shift resulted in increased efficiency as shown in [6].

We believe that future requirements for water turbines will emphasize flexibility. For this reason, the future research on cavitation in water turbines will focus on the minimization of cavitation occurrence and erosion, while at the same time providing adequate energy output and efficiency.

Author Contributions: Conceptualization, A.P., M.H. and M.D.; methodology, A.P., M.H., L.N. and M.D.; software, A.P. and L.N.; validation, A.P., M.H., L.N. and M.D.; formal analysis, A.P., M.H. and L.N.; investigation, A.P., M.H., L.N. and M.D.; resources, A.P., M.H. and M.D.; data curation, A.P., M.H. and L.N.; writing—original draft preparation, A.P. and M.H.; writing—review and editing, A.P., M.H., L.N. and M.D.; visualization, A.P. and M.H.; supervision, M.H. and M.D.; project administration, A.P. and M.H.; funding acquisition, M.H. and M.D. All authors have read and agreed to the published version of the manuscript.

Funding: This study was performed with financial support of Research Program P2-0401 Energy Engineering from Slovenian Research Agency ARRS.

Institutional Review Board Statement: Not applicable.

Informed Consent Statement: Not applicable.

Conflicts of Interest: The authors declare no conflict of interest.

References

1. Platero, C.A.; Sánchez, J.A.; Nicolet, C.; Allenbach, P. Hydropower plants frequency regulation depending on upper reservoir water level. *Energies* **2019**, *12*, 1637. [[CrossRef](#)]
2. Yang, W.; Yang, J.; Guo, W.; Norrlund, P. Response time for primary frequency control of hydroelectric generating unit. *Int. J. Electr. Power Energy Syst.* **2016**, *74*, 16–24. [[CrossRef](#)]

3. Denholm, P.; O'Connell, M.; Brinkman, G.; Jorgenson, J. *Overgeneration from Solar Energy in California: A Field Guide to the Duck Chart (NREL/TP-6A20-65023)*; National Renewable Energy Laboratory: Golden, CO, USA, 2015.
4. Presas, A.; Valentin, D.; Egusquiza, E.; Valero, C. Detection and analysis of part load and full load instabilities in a real Francis turbine prototype. In *Proceedings of the Journal of Physics: Conference Series*; IOP Publishing: Bristol, UK, 2017; Volume 813.
5. Vagnoni, E.; Favrel, A.; Andolfatto, L.; Avellan, F. Experimental investigation of the sloshing motion of the water free surface in the draft tube of a Francis turbine operating in synchronous condenser mode. *Exp. Fluids* **2018**, *59*, 95. [[CrossRef](#)]
6. Podnar, A.; Dular, M.; Širok, B.; Hočevár, M. Experimental Analysis of Cavitation Phenomena on Kaplan Turbine Blades Using Flow Visualization. *J. Fluids Eng.* **2019**, *141*. [[CrossRef](#)]
7. Avellan, F. Introduction to cavitation in hydraulic machinery. In *Proceedings of the 6th Int. Conf. on Hydraulic Machinery and Hydrodynamics*; Politehnica University of Timișoara: Timișoara, Romania, 2004; pp. 11–22.
8. Asuaje, M.; Bakir, F.; Kouidri, S.; Rey, R. Inverse Design Method for Centrifugal Impellers and Comparison with Numerical Simulation Tools. In *Proceedings of the International Journal of Computational Fluid Dynamics*; Taylor & Francis: Abingdon-on-Thames, UK, 2004; Volume 18, pp. 101–110.
9. Wu, J.; Shimmei, K.; Tani, K.; Niikura, K.; Sato, J. CFD-based design optimization for hydro turbines. *J. Fluids Eng. Trans. ASME* **2007**, *129*, 159–168. [[CrossRef](#)]
10. Zangeneh, M. A compressible three-dimensional design method for radial and mixed flow turbomachinery blades. *Int. J. Numer. Methods Fluids* **1991**, *13*, 599–624. [[CrossRef](#)]
11. Zhu, B.; Wang, X.; Tan, L.; Zhou, D.; Zhao, Y.; Cao, S. Optimization design of a reversible pump-turbine runner with high efficiency and stability. *Renew. Energy* **2015**, *81*, 366–376. [[CrossRef](#)]
12. Leguizamón, S.; Avellan, F. Open-source implementation and validation of a 3D inverse design method for Francis turbine runners. *Energies* **2020**, *13*, 2020. [[CrossRef](#)]
13. Daneshkahi, K.; Zangeneh, M. Parametric design of a Francis turbine runner by means of a three-dimensional inverse design method. *IOP Conf. Ser. Earth Environ. Sci.* **2010**, *12*, 012058. [[CrossRef](#)]
14. Olimstad, G.; Nielsen, T.; Børresen, B. Dependency on runner geometry for reversible-pump turbine characteristics in turbine mode of operation. *J. Fluids Eng. Trans. ASME* **2012**, *134*. [[CrossRef](#)]
15. Xue, P.; Liu, Z.P.; Lu, L.; Tian, Y.J.; Wang, X.; Chen, R. Research and optimization of performances of a pump turbine in pump mode. In *Proceedings of the IOP Conference Series: Earth and Environmental Science*; IOP Publishing: Bristol, UK, 2019; Volume 240.
16. Ma, Z.; Zhu, B.; Rao, C.; Shangguan, Y. Comprehensive hydraulic improvement and parametric analysis of a Francis turbine runner. *Energies* **2019**, *12*, 307. [[CrossRef](#)]
17. Lemay, S.; Aeschlimann, V.; Fraser, R.; Ciocan, G.D.; Deschênes, C. Velocity field investigation inside a bulb turbine runner using endoscopic PIV measurements. *Exp. Fluids* **2015**, *56*. [[CrossRef](#)]
18. International Electrotechnical Commission. *IEC60193 Hydraulic Turbines, Storage Pumps and Pump-Turbines-Model Acceptance Tests*; BSI Br. Standards; BSI Group: London, UK, 1999.
19. Riegels, F.W. *Aerodynamische Profile*; Oldenbourg: München, Germany, 1958.
20. Althaus, D. *Stuttgarter Profilkatalog 1*; Institut für Aerodynamik und Gasdynamik der Universität Stuttgart: Stuttgart, Germany, 1972.
21. Frikha, S.; Coutier-Delgosha, O.; Astolfi, J.A. Influence of the cavitation model on the simulation of cloud cavitation on 2D foil section. *Int. J. Rotating Mach.* **2008**, *2008*. [[CrossRef](#)]
22. Širok, B.; Dular, M.; Stoffel, B. *Kavitacija*; i2: Ljubljana, Slovenia, 2006; ISBN 9616348310. 9789616348317.
23. Chanson, H. Advective diffusion of air bubbles in turbulent water flows. In *Fluid Mechanics of Environmental Interfaces*; Taylor & Francis: Leiden, The Netherlands, 2008; Volume 219, pp. 163–196. ISBN 9781134064236.
24. Deveaux, B.; Fournis, C.; Brion, V.; Marty, J.; Dazin, A. Experimental analysis and modeling of the losses in the tip leakage flow of an isolated, non-rotating blade setup. *Exp. Fluids* **2020**, *61*. [[CrossRef](#)]
25. Brennen, C.E. *Cavitation and Bubble Dynamics*; Oxford University Press: New York, NY, USA, 1994.
26. Brennen, C.E. *Fundamentals of Multiphase Flow*; Cambridge University Press: Cambridge, UK, 1995; ISBN 9780511807169.
27. Bajcar, T.; Širok, B.; Eberlinc, M. Quantification of flow kinematics using computer-aided visualization. *Stroj. Vestnik/J. Mech. Eng.* **2009**, *4*, 215–223.